


Crystallographic dependence of the spin Hall angle in epitaxial Pt films: Comparison of optical and electrical detection of spin-torque ferromagnetic resonance techniques

F

Cite as: Appl. Phys. Lett. **120**, 172406 (2022); <https://doi.org/10.1063/5.0085818>
 Submitted: 19 January 2022 • Accepted: 25 March 2022 • Published Online: 28 April 2022

 Bharat Grover,  Binoy Krishna Hazra, Tianping Ma, et al.

COLLECTIONS

 This paper was selected as Featured



View Online



Export Citation



CrossMark

ARTICLES YOU MAY BE INTERESTED IN

[Observation of domain structure in non-collinear antiferromagnetic Mn₃Sn thin films by magneto-optical Kerr effect](#)

Applied Physics Letters **120**, 172405 (2022); <https://doi.org/10.1063/5.0089355>

[Nanosecond ultralow power spin orbit torque magnetization switching driven by BiSb topological insulator](#)

Applied Physics Letters **120**, 152401 (2022); <https://doi.org/10.1063/5.0084927>

[A perspective on electrical generation of spin current for magnetic random access memories](#)

Applied Physics Letters **120**, 160502 (2022); <https://doi.org/10.1063/5.0084551>

 QBLOX



1 qubit

Shorten Setup Time
Auto-Calibration
More Qubits

Fully-integrated
Quantum Control Stacks
Ultrastable DC to 18.5 GHz
 Synchronized <<1 ns
 Ultralow noise



100s qubits

[visit our website >](#)

Crystallographic dependence of the spin Hall angle in epitaxial Pt films: Comparison of optical and electrical detection of spin-torque ferromagnetic resonance techniques

Cite as: Appl. Phys. Lett. **120**, 172406 (2022); doi: [10.1063/5.0085818](https://doi.org/10.1063/5.0085818)

Submitted: 19 January 2022 · Accepted: 25 March 2022 ·

Published Online: 28 April 2022



View Online



Export Citation



CrossMark

Bharat Grover,^{1,2,a)}  Binoy Krishna Hazra,¹  Tianping Ma,^{1,2} Banabir Pal,¹ Nirel Bernstein,³  Amit Rothschild,³ Abhay Kant Srivastava,¹ Samiran Choudhury,¹ Georg Woltersdorf,^{1,2}  Amir Capua,³  and Stuart S. P. Parkin^{1,2,a)} 

AFFILIATIONS

¹Max Planck Institute for Microstructure Physics, 06120 Halle, Germany

²Institute of Physics, Martin Luther University Halle-Wittenberg, 06120 Halle, Germany

³The Hebrew University of Jerusalem, Jerusalem 9190401, Israel

^{a)}Authors to whom correspondence should be addressed: bhgrover@mpi-halle.mpg.de and stuart.parkin@mpi-halle.mpg.de

ABSTRACT

The spin Hall effect appears in nature in two forms. Its intrinsic form is highly dependent on the crystal symmetry while its extrinsic form stems from impurity scattering. Its efficiency is defined by the spin Hall angle, θ_{SH} , and has profound impact on spintronic technologies. However, an accurate measurement of θ_{SH} is not straightforward nor the identification of its origin. In this work, we apply a spin-torque driven ferromagnetic resonance method that is probed in two different ways, optically and electrically, to study the dependence of θ_{SH} in the crystallographic direction in epitaxial $\text{Al}_2\text{O}_3/\text{Pt}$ (111), $\text{MgO}(110)/\text{Pt}$ (110), and $\text{MgO}(001)/\text{Pt}$ (001) films. We show that the electrical technique is limited in its ability to accurately quantify θ_{SH} at high current densities, and in some cases, it may even result in erroneous θ_{SH} values. Such cases include films that exhibit a large inhomogeneous broadening. We find that θ_{SH} is strongly affected by the crystallographic direction. Our study extends the understanding of one of the most commonly used methods for the exploration of the spin Hall effect.

© 2022 Author(s). All article content, except where otherwise noted, is licensed under a Creative Commons Attribution (CC BY) license (<http://creativecommons.org/licenses/by/4.0/>). <https://doi.org/10.1063/5.0085818>

The spin Hall effect (SHE) is a collection of relativistic phenomena, where charge current j_c can generate a transverse spin current $j_s \frac{\hbar}{2e}$ through spin-orbit coupling (SOC).¹ In recent years, the SHE has proven useful in manipulating the magnetization order parameter in perpendicularly magnetized ferromagnets (FMs)² and in antiferromagnets³ for applications such as magnetic logic and storage devices.⁴ The SHE is also fundamentally interesting as it stems from a scattering process in a well-defined band structure. The scattering mechanisms are closely related to those dominating the anomalous Hall effect (AHE). Therefore, the extrinsic contribution to the spin Hall conductivity (σ_{xy}^{SH}) depends on the scattering rate (τ) of the electron's spin. While the extrinsic contribution to σ_{xy}^{SH} scales linearly with longitudinal conductivity (σ_{xx}) (or τ), the intrinsic process is independent of τ and arises from the band structure of the crystal, its symmetries, and orientation.^{5–7}

Pt in its various forms is one of the most important metals for exploration of the SHE owing to the high strength of its SOC.⁸ It is

generally understood that the SHE in Pt arises from both intrinsic and extrinsic contributions.⁹ In polycrystalline films, the resistivity and the temperature dependence of the SHE have been used to distinguish between these origins.¹⁰ However, studies of the SHE in epitaxial films,^{7,11} where the intrinsic SHE should be more important, are less common.

In addition to the challenges that are related to the fabrication and engineering of the materials, the accurate determination of the spin Hall angle, θ_{SH} , also impedes the development of SHE based technologies. Among a variety of techniques, the spin torque driven ferromagnetic resonance (STFMR)¹² technique has been extensively used to determine θ_{SH} . In a typical measurement, an RF electrical current is passed through a heavy metal/ferromagnet (HM/FM) bilayer where spins are polarized by the HM layer and diffuse into the FM layer. By interaction with the local magnetic moments, an RF spin-torque excites the ferromagnetic resonance (FMR) of the FM layer that is

sensed by measuring a DC voltage (V_{mix}) across the device. V_{mix} is a result of the interplay between the oscillatory anisotropic magnetoresistance (AMR) effect¹² and the RF current. The θ_{SH} is determined by passing an additional DC that modulates the damping of the FM.¹³

Despite its simplicity, interpreting the signal of the STFMR requires careful analysis.^{14,15} In addition to the RF spin-torque, there is also an RF Oersted torque that is generated from the RF current. Furthermore, V_{mix} can have additional contributions. First, spin pumping by the FM into the HM generates an electrical voltage via the inverse SHE.¹⁶ Second, an anomalous Hall voltage is also present due to the flow of the charge current.¹⁴ Finally, thermoelectric effects, such as the longitudinal spin Seebeck and Nernst effects,¹⁷ exist as well.

In this work, we explore the SHE in epitaxial Pt thin films. We explore the role of the crystallographic orientation. In addition to the STFMR measurements, we also use an optically detected spin-torque driven FMR (O-STFMR) method where the magnetization is probed via the magneto-optical Kerr effect (MOKE)¹⁸ rather than by measuring V_{mix} . From a comparison of the two methods, we find that the DC voltage applied to the sample may add an artifact to the electrical measurements. In some cases, an incorrect θ_{SH} may result even when the FMR signal is readily resolved. We find that the O-STFMR benefits from a higher sensitivity that enables to explore the SHE in the presence of stronger DC spin-torques as compared to the STFMR. Hence, the role of the crystallographic directions can be resolved with high fidelity. The films were grown by DC magnetron sputtering in a vacuum system that has a base pressure of $\sim 1 \times 10^{-9}$ Torr. Pt (111) and Pt (110) layers were sputtered at 550 °C directly onto Al_2O_3 (0001) and MgO (110) substrates, respectively, whereas Pt (001) was grown at 650 °C on a 0.3 nm thick Fe buffered MgO (001) substrate. The

sputtering power and Ar pressure were 30 W and 3 mTorr, respectively. The thickness of the Pt layer is ~ 5 nm in all films. A 5 nm thick FM layer formed from Py ($\text{Ni}_{81}\text{Fe}_{19}$) was grown at room temperature on top of the different Pt films at a sputtering power of 30 W and an Ar pressure of 3 mTorr. We use the notation Pt (111), Pt (110), and Pt (001) to indicate the Al_2O_3 (0001)/Pt/Py, MgO (110)/Pt/Py, and MgO (001)/Fe/Pt/Py films unless specified otherwise. All films were capped with a 3 nm thick TaN layer to prevent oxidation. Figure 1(a) shows specular $\theta-2\theta$ longitudinal x-ray diffraction (XRD) data. The (111), (110), and (001) peaks of Pt are readily seen indicating the high degree of crystalline texture of the films. Additionally, well-resolved thickness fringes are observed in the Pt (111) film illustrating the higher quality of Pt (111) as compared to the Pt (110) and Pt (001) films. The surface roughness of Pt (111) and Pt (001) was comparable and having relatively low values of 0.6 and 0.4 nm, respectively, whereas Pt (110) had a roughness of 1.8 nm as seen in the atomic force microscopy (AFM) data presented in the supplementary material. A similar observation was made in Ref. 19 with the exact reason for being unclear. In order to accurately determine θ_{SH} , the resistivity of the single Pt layer was extracted by growing additional Pt/TaN films with the respective crystal orientations. The resistivity values were 18 ± 1 , 30 ± 4 , and $33 \pm 1 \mu\Omega\text{-cm}$ for the bare Pt (111), Pt (110), and Pt (001) layers, respectively, and did not reflect the large surface roughness of Pt (110). However, the surface roughness was reflected in the in-plane MOKE hysteresis curves. Figure 1(b) readily shows that the MOKE signal of Pt (110) is weaker by more than 50% as compared to the other orientations. Also, the switching transition of Pt/Py (111) and Pt/Py (001) is sharper suggesting a more homogeneous magnetization texture in these films.

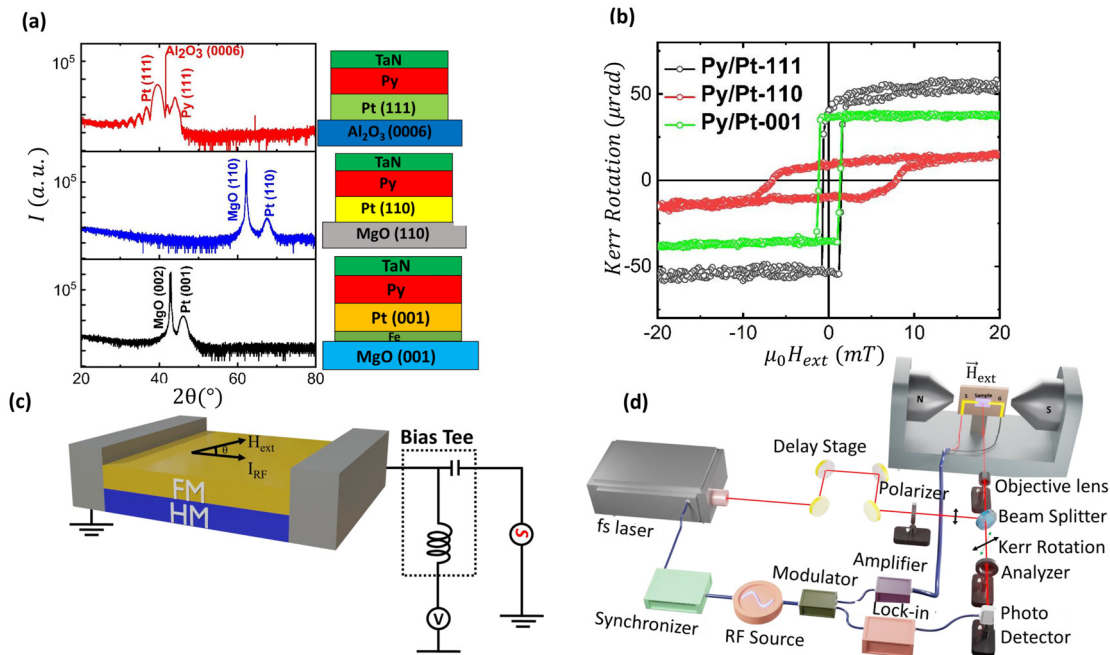


FIG. 1. (a) XRD data of Pt (111), Pt (110), and Pt(001) samples. (b) In-plane MOKE hysteresis loops for Pt (111), Pt (110), and Pt(001). (c) Schematic illustration of the STFMR setup. (d) Schematic illustration of the O-STFMR setup.

The O-STFMR and STFMR measurements were performed on the same devices. The samples were patterned by optical lithography followed by Ar ion-milling to define devices of area $25 \times 50 \mu\text{m}^2$. The conventional STFMR setup used in this work is described in Ref. 9 with an external magnetic field applied at 45° with respect to the current and V_{mix} directions as illustrated in Fig. 1(c).

The O-STFMR setup is presented in Fig. 1(d). A 35 fs Ti:Sapphire laser operating at 800 nm and a repetition rate of 80 MHz was used to probe the magnetization precession using the perpendicular MOKE configuration, which senses the out-of-plane component of the magnetization, m_z . To that end, the laser was phase-locked with the driving RF microwave signal that was passed through the sample as in the STFMR technique. An optical delay line allows for the accurate control of the timing of the incident pulses with respect to the magnetization precession. In contrast to the STFMR, the O-STFMR is sensitive to both the phase and amplitude of m_z . The external magnetic field, H_{ext} , was applied in the sample plane at 45° with respect to the direction of the current similar to the STFMR setup. In both techniques, θ_{SH} was extracted from DC bias dependent FMR linewidth measurements.

Figure 2 presents an example of the measured STFMR and O-STFMR spectra of the Pt (111) sample at 6–13 and 6.2–13.5 GHz, respectively. Each STFMR spectrum is composed of symmetric and anti-symmetric signals that stem, respectively, from the spin-orbit torque (SOT) and Oersted field contributions.^{12,15} In contrast, the O-STFMR measurement is phase sensitive. The spectral line shape depends on the ratio of the in-phase to out-of-phase components of the susceptibility (χ' and χ''), which is determined by the timing of the pulses relative to RF excitation. At each frequency, the relative timing is different, hence, also the symmetry as seen in Fig. 2(b). To extract the resonance field and linewidth, each trace was decomposed into the symmetric and anti-symmetric parts similar to the procedure applied for STFMR measurements.¹⁵

The resonance field, H_{res} , and the linewidth, ΔH , can be determined in the STFMR and O-STFMR responses by fitting the measured spectra to a sum of symmetric and anti-symmetric Lorentzian functions according to

$$V_{E/O} = V_{S_{E/O}} \frac{\Delta H^2}{[(H - H_{\text{res}})^2 + \Delta H^2]} + V_{A_{E/O}} \frac{(H - H_{\text{res}})\Delta H}{[(H - H_{\text{res}})^2 + \Delta H^2]}, \quad (1)$$

where V_S and V_A are the symmetric and anti-symmetric parts of the Lorentzian, respectively, and the sub-index E or O indicates the electrical STFMR or optical O-STFMR method. The extracted frequency dispersion curves are summarized in Figs. 3(a) and 3(b) for the STFMR and O-STFMR measurements, respectively. The traces obtained by both methods are similar. Using the Kittel formula, $f = \frac{\mu_0 \gamma}{2\pi} \sqrt{(H_{\text{res}} + H_k)(H_{\text{res}} + M_{\text{eff}} + H_k)}$, an effective magnetization, $\mu_0 M_{\text{eff}} \sim 1012 \pm 2 \text{ mT}$ ($993 \pm 4 \text{ mT}$), $700 \pm 6 \text{ mT}$ ($732 \pm 10 \text{ mT}$), and $968 \pm 3 \text{ mT}$ ($970 \pm 1 \text{ mT}$) was extracted for the Pt (111), Pt (110), and Pt (001) films, respectively, using the STFMR (O-STFMR). H_k was negligible in Pt-(111) and Pt(001) but significant in Pt (110), where it was $19 \pm 0.2 \text{ mT}$ ($22 \pm 0.1 \text{ mT}$) as extracted by the STFMR (O-STFMR). γ and μ_0 are the gyromagnetic ratio and the magnetic permeability of free space, respectively. We use the literature value for γ of Permalloy = 178 GHz/T. M_{eff} for the Pt (110) film appears to be lower by $\sim 30\%$ as compared to the values for Pt (111) and Pt (001). Additionally, the M_{eff} values as measured by the optical and electrical methods for Pt (111) and Pt (001) agree within an error that is smaller than 1% while the difference for Pt (110) is significantly larger, reaching almost 5%. We attribute this behavior to the surface roughness. The same trend was also seen in the saturation magnetization, M_S , values measured by a vibrating sample magnetometer (VSM) (VSM data presented in the [supplementary material](#)).

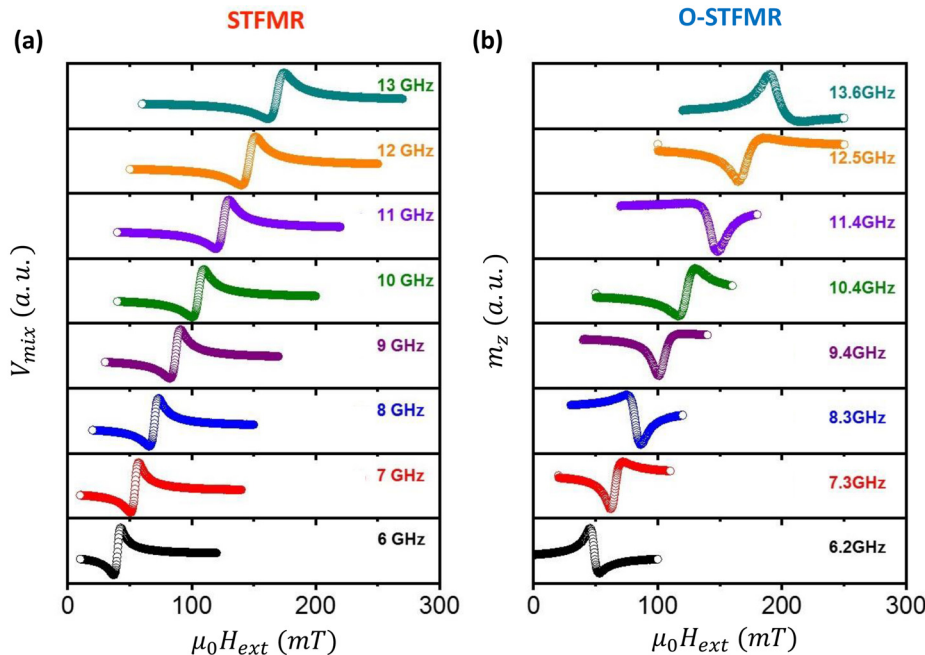


FIG. 2. Examples of measured spectra for a device fabricated from Al_2O_3 (0001)/Pt/Py at RF frequencies from 6 to 13.5 GHz. (a) STFMR and (b) O-STFMR spectra.

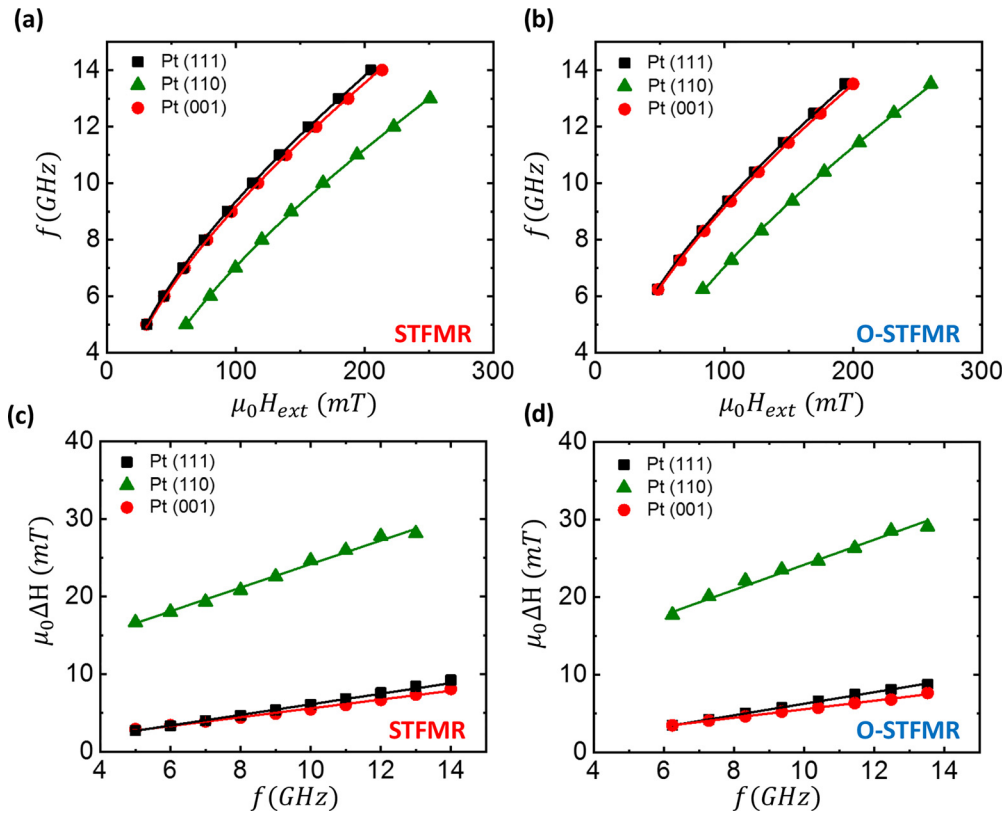


FIG. 3. (a) Frequency dispersion curves measured by (a) STFM and (b) O-STFM. Linewidth measurements obtained by (c) STFM and (d) O-STFM.

The Gilbert damping parameter, α was extracted from ΔH measurements using the relation $\mu_0 \Delta H = \mu_0 \Delta H_0 + 2\pi\alpha f / \gamma$. ΔH_0 arises from inhomogeneous broadening and disorder in the crystalline structure. Figures 3(c) and 3(d) present the measurements of ΔH . The α values obtained are $19.28 \pm 0.35 \times 10^{-3}$ ($20.9 \pm 0.2 \times 10^{-3}$), $42.86 \pm 1.0 \times 10^{-3}$ ($45.7 \pm 2 \times 10^{-3}$), and $16.08 \pm 0.1 \times 10^{-3}$ ($15.4 \pm 0.2 \times 10^{-3}$) for Pt (111), Pt (110), and Pt (001), respectively, extracted using the STFM (O-STFM). These values are consistent with other reports.²⁰ Despite the larger values of α for the Pt (110) sample, both the optical and electrical methods result in very similar values. It is possible that the Pt–Py interface of Pt (110) is more dominant in Pt (110) giving rise to efficient spin pumping through the interface and the appearance of significant H_k . The ΔH_0 values extracted were 0.1 ± 0.15 mT (0.07 ± 0.06 mT), 9 ± 0.50 mT (8 ± 0.6 mT), and 0.7 ± 0.08 mT (1.1 ± 0.07 mT) for Pt (111), Pt (110), and, Pt (001), as measured by the STFM (O-STFM), respectively. Here as well, the STFM and O-STFM methods agree very well. The large ΔH_0 value of Pt (110) as compared to the other orientations illustrates quantitatively the conclusions drawn from the qualitative analysis of the static MOKE and the influence of the surface roughness on the measured magnetization dynamics.

θ_{SH} was quantified from DC bias linewidth modulation measurements. The spin current density flowing in the Pt layer, J_S , generates DC spin currents that modulate ΔH of the Py by a damping/anti-damping SOT. The resultant effective damping, α_{eff} , is linearly dependent on J_S as follows:²¹

$$\alpha_{eff} = \alpha + \frac{\sin \varphi}{(\mu_0 H_{res} + 0.5 M_{eff}) \mu_0 M_{St}} \frac{\hbar J_S}{2e}. \quad (2)$$

In Eq. (2), φ is the angle between the charge current and the externally applied field, which is 45° in both techniques, and t is the thickness of the Py layer. Equation (2) can be written more conveniently from which θ_{SH} can be extracted as follows:

$$\theta_{SH} = \frac{\partial(\delta \Delta H) / \partial(I_{DC})}{\frac{2\pi f}{\gamma} \left[\frac{\sin \varphi}{(\mu_0 H_{res} + 0.5 M_{eff}) \mu_0 M_{St}} \right] \frac{\hbar}{2e}} \left[\frac{\rho_{Py} t_{Pt} + \rho_{Pt} t_{Py}}{\rho_{Py}} \right] \cdot w. \quad (3)$$

In Eq. (3), I_{DC} is the bias current, and $\delta \mu_0 \Delta H$ is the variation in $\mu_0 \Delta H$ as a result of I_{DC} . ρ_{Pt} and ρ_{Py} are the resistivities of Pt and Py, respectively, and w is the width of the device. From Eqs. (2) and (3), it is seen that when the external field is reversed, $\sin \varphi$ changes sign so that the dependence of ΔH on I_{DC} is also reversed.

I_{DC} dependent linewidth data at 6 GHz are presented in Fig. 4. The linear dependence of $\delta \mu_0 \Delta H$ on I_{DC} is readily seen. Additionally, it is seen that the maximal applicable current in the optical measurements is nearly four times larger as compared to the electrical STFM. We understand this limitation to arise from the AMR together with the fact that the external magnetic field is applied at 45° . Due to a small but finite shape anisotropy, as the external magnetic field is swept, the magnetization slightly varies its orientation. As a result, the

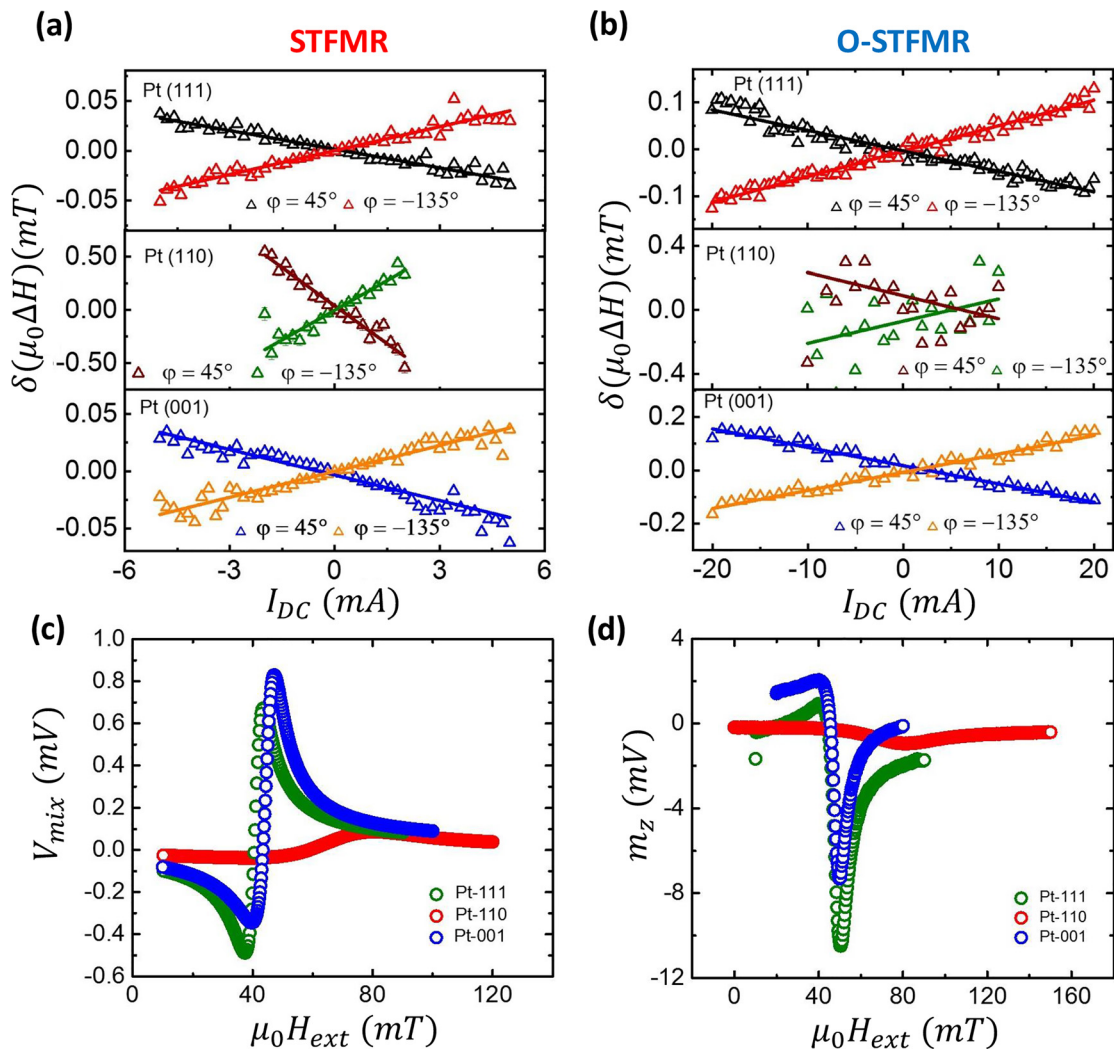


FIG. 4. Current dependent linewidth broadening at 6 GHz for Pt (111), Pt (110), and Pt (001). (a) STFMR measurements. (b) O-STFMR measurements. (c) STFMR and (d) O-STFMR zero bias spectra for Pt (111), Pt (110), and Pt (001).

DC resistance slightly varies as well. When I_{DC} is applied these variations translate to a field dependent DC voltage that becomes larger as I_{DC} increases. This field dependent background signal complicates the analysis of the STFMR signal at high currents. In contrast, the O-STFMR is independent of the AMR, and I_{DC} dependent damping can be studied over a wider range of currents. Hence, θ_{SH} can be quantified more accurately. Operation at higher frequencies and fields may, in principle, resolve this issue of the STFMR method, but in practice, the signal to noise (SNR) would also reduce. STFMR measurements at 8 GHz are presented in the [supplementary material](#) as an example.

Surprisingly, the O-STFMR linewidth modulation data of Pt (110) are much noisier than the STFMR data, while the latter reveals a clear linear dependence on I_{DC} . The θ_{SH} values explain this contradiction. θ_{SH} for Pt (111) and Pt (001) are 0.053 ± 0.01 (0.043 ± 0.01) and 0.072 ± 0.01 (0.068 ± 0.01) as measured by the STFMR (O-STFMR),

respectively. (Error analysis is presented in the [supplementary material](#).) Namely, both methods result in relatively close θ_{SH} . In contrast, θ_{SH} extracted for Pt (110) reveals a big discrepancy: an extraordinarily large θ_{SH} of 0.45 ± 0.2 is extracted using the STFMR while the O-STFMR results in 0.09 ± 0.03 . Additionally, it is seen that all θ_{SH} values obtained by the STFMR are larger than those obtained using the O-STFMR. These observations indicate a measurement artifact of the STFMR. Once again, the AMR may explain this behavior. The H_{ext} dependent background signal becomes critical the weaker and broader the signal is. The FMR signal of Pt (110) is weaker by almost an order of magnitude as illustrated in [Figs. 4\(c\) and 4\(d\)](#). Hence, the AMR H_{ext} dependent background voltage strongly influences the Pt (110) sample that eventually translates to a measurement artifact and a $\theta_{SH} \sim 0.45$. The other films less are not as affected by this artifact as their SNR is much higher; nevertheless, a θ_{SH} that is higher by 20%

TABLE I. Summary of θ_{SH} for Pt (111), Pt (110), Pt (001), and textured Pt (Pt/Si) films measured by O-STFMR and STFMR.

Sample	θ_{SH} (O-STFMR)	θ_{SH} (STFMR)	Intrinsic θ_{SH} (O-STFMR)	Intrinsic θ_{SH} (STFMR)
Pt-111	0.043 ± 0.01	0.053 ± 0.01	0.089 ± 0.01	0.109 ± 0.01
Pt-110	0.09 ± 0.03	0.45 ± 0.2	NA	NA
Pt-001	0.068 ± 0.01	0.072 ± 0.01	0.107 ± 0.01	0.113 ± 0.02
Pt/Si	0.08 ± 0.01	0.09 ± 0.01	0.12 ± 0.01	0.14 ± 0.01

results. Overall, we conclude that θ_{SH} is ~ 0.043 , ~ 0.09 , and ~ 0.068 for the Pt (111), Pt (110), and Pt (001) films, respectively, as measured by the O-STFMR. Using Ref. 20, we also estimated the transparency of the Pt-Py interface from which the intrinsic θ_{SH} was extracted having the values of 0.089 ± 0.01 and 0.107 ± 0.01 for Pt (111) and Pt (001), respectively. The model could not be applied in the case of Pt (110) due to its high damping. Table I presents a summary of all θ_{SH} values.

The crystallographic direction in Pt can significantly influence the SHE. As a reference, we grew a textured Pt film along the (111) direction of the same structure: Si/SiO₂/5 Pt/5 Py (units in nm). This Pt film had a resistivity of $27 \pm 2 \mu\Omega\text{-cm}$, an α of $(14.0 \pm 0.1) \times 10^{-3}$, and a $\mu_0 * \Delta H_0$ of $1.15 \pm 0.3 \text{ mT}$ that resulted in a value of θ_{SH} of 0.09 ± 0.01 (0.08 ± 0.01) measured using STFMR (O-STFMR) and an intrinsic θ_{SH} of 0.14 ± 0.01 (0.12 ± 0.01). Once again, θ_{SH} of the STFMR is larger than that obtained using the O-STFMR. The conversion rate of the textured Pt is higher as compared to the average of the three epitaxial crystals, which may indicate additional extrinsic contribution to θ_{SH} . Finally, we also have examined the field like torque efficiency ζ_{FL} following Ref. 22, revealing a very small contribution of ζ_{FL} . This study is presented in the [supplementary material](#).

In summary, in this work, we have explored the SHE in epitaxial Pt films using electrical and optical detection. We identified the AMR of the STFMR as the limiting factor in cases of low SNR. Most importantly, the case where the STFMR signal is weak but still observable can lead to an erroneous measurement. Moreover, we demonstrated that the conversion of the charge to spin current can be measured at much higher applied currents using O-STFMR as compared to that using STFMR. The comparison of the various methods is important in identifying the underlying physics of the SHE.

See the [supplementary material](#) for VSM, AFM Data, parameters used for θ_{SH} calculation, field like torque analysis, etc.

AUTHOR DECLARATIONS

Conflict of Interest

The authors have no conflicts to disclose.

DATA AVAILABILITY

The data that support the findings of this study are available from the corresponding authors upon reasonable request.

REFERENCES

- J. Sinova, S. O. Valenzuela, J. Wunderlich, C. H. Back, and T. Jungwirth, "Spin Hall effects," *Rev. Mod. Phys.* **87**(4), 1213 (2015).
- J. Kim, J. Sinha, M. Hayashi, M. Yamanouchi, S. Fukami, T. Suzuki, S. Mitani, and H. Ohno, "Layer thickness dependence of the current-induced effective field vector in Ta|CoFeB|MgO," *Nat. Mater.* **12**(3), 240–245 (2013).
- H. Tsai, T. Higo, K. Kondou, T. Nomoto, A. Sakai, A. Kobayashi, T. Nakano, K. Yakushiji, R. Arita, and S. Miwa, "Electrical manipulation of a topological antiferromagnetic state," *Nature* **580**(7805), 608–613 (2020).
- H. Dery, P. Dalal, L. Cywiński, and L. J. Sham, "Spin-based logic in semiconductors for reconfigurable large-scale circuits," *Nature* **447**(7144), 573–576 (2007).
- L. Zhu, D. C. Ralph, and R. A. Buhrman, "Maximizing spin-orbit torque generated by the spin Hall effect of Pt," *Appl. Phys. Rev.* **8**(3), 031308 (2021).
- N. Nagaosa, J. Sinova, S. Onoda, A. H. MacDonald, and N. P. Ong, "Anomalous Hall effect," *Rev. Mod. Phys.* **82**(2), 1539–1592 (2010).
- L. Zhu, L. Zhu, M. Sui, D. C. Ralph, and R. A. Buhrman, "Variation of the giant intrinsic spin Hall conductivity of Pt with carrier lifetime," *Sci. Adv.* **5**(7), eaav8025 (2019).
- G. Y. Guo, S. Murakami, T.-W. Chen, and N. Nagaosa, "Intrinsic spin Hall effect in platinum: First-principles calculations," *Phys. Rev. Lett.* **100**(9), 096401 (2008).
- R. Freeman, A. Zholud, Z. Dun, H. Zhou, and S. Urazhdin, "Evidence for Dyakonov-Perel-like spin relaxation in Pt," *Phys. Rev. Lett.* **120**(6), 067204 (2018).
- Y. Wang, P. Deorani, X. Qiu, J. H. Kwon, and H. Yang, "Determination of intrinsic spin Hall angle in Pt," *Appl. Phys. Lett.* **105**(15), 152412 (2014).
- C. Garg, S.-H. Yang, L. Thompson, T. Topuria, A. Capua, B. i. a. Hughes, T. Phung, P. C. Filippou, and S. S. Parkin, "Efficient chiral-domain-wall motion driven by spin-orbit torque in metastable platinum films," *Phys. Rev. Appl.* **14**(3), 034052 (2020).
- L. Liu, T. Moriyama, D. C. Ralph, and R. A. Buhrman, "Spin-torque ferromagnetic resonance induced by the spin Hall effect," *Phys. Rev. Lett.* **106**(3), 036601 (2011).
- Y. Wang, R. Ramaswamy, and H. Yang, "FMR-related phenomena in spintronic devices," *J. Phys. D* **51**(27), 273002 (2018).
- Y. Zhang, Q. Liu, B. F. Miao, H. F. Ding, and X. R. Wang, "Anatomy of electrical signals and dc-voltage line shape in spin-torque ferromagnetic resonance," *Phys. Rev. B* **99**(6), 064424 (2019).
- R. Ben-Shalom, N. Bernstein, S. S. P. Parkin, S.-H. Yang, and A. Capua, "Determination of the spin Hall angle by the inverse spin Hall effect, device level ferromagnetic resonance, and spin torque ferromagnetic resonance: A comparison of methods," *Appl. Phys. Lett.* **119**(4), 042401 (2021).
- E. Saitoh, M. Ueda, H. Miyajima, and G. Tatara, "Conversion of spin current into charge current at room temperature: Inverse spin-Hall effect," *Appl. Phys. Lett.* **88**(18), 182509 (2006).
- K.-D. Lee, D.-J. Kim, H. Yeon Lee, S.-H. Kim, J.-H. Lee, K.-M. Lee, J.-R. Jeong, K.-S. Lee, H.-S. Song, J.-W. Sohn, S.-C. Shin, and B.-G. Park, "Thermoelectric signal enhancement by reconciling the spin Seebeck and anomalous Nernst effects in ferromagnet/non-magnet multilayers," *Sci. Rep.* **5**(1), 10249 (2015).
- Z. Q. Qiu and S. D. Bader, "Surface magneto-optic Kerr effect (SMOKE)," *J. Magn. Magn. Mater.* **200**(1–3), 664–678 (1999).
- Y. Tolstova, S. T. Omelchenko, A. M. Shing, and H. A. Atwater, "Heteroepitaxial growth of Pt and Au thin films on MgO single crystals by bias-assisted sputtering," *Sci. Rep.* **6**(1), 23232 (2016).
- W. Zhang, W. Han, X. Jiang, S.-H. Yang, and S. S. P. Parkin, "Role of transparency of platinum-ferromagnet interfaces in determining the intrinsic magnitude of the spin Hall effect," *Nat. Phys.* **11**(6), 496–502 (2015).
- S. Petit, C. Baraduc, C. Thirion, U. Ebels, Y. Liu, M. Li, P. Wang, and B. Dieny, "Spin-torque influence on the high-frequency magnetization fluctuations in magnetic tunnel junctions," *Phys. Rev. Lett.* **98**(7), 077203 (2007).
- C. Kim, D. Kim, B. S. Chun, K.-W. Moon, and C. Hwang, "Evaluation method for Fieldlike-torque efficiency by modulation of the resonance field," *Phys. Rev. Appl.* **9**(5), 054035 (2018).